# Efficient Carbon Counter Electrodes for BaSnO$_3$-based Dye-Sensitized Solar Cells

Anurag Roy[a,b,*], Puja Ghosh[a], Parukuttyamma Sujatha Devi[a,c], Senthilarasu Sundaram[b] and Tapas K. Mallick[b]

[a]*Functional Materials and Devices Divison, CSIR-Central Glass and Ceramic Research Institute, 196 Raja S.C. Mullick Road, Jadavpur, Kolkata 700032, India*
[b]*Environment and Sustainability Institute, University of Exeter, Penryn Campus, Cornwall TR10 9FE, U.K*
[c]*Chemical Science and Technology Division, CSIR-National Institute for Interdisciplinary Science and Technology, Thiruvananthapuram, Kerala 695019, India*

## Abstract

Natural source derived carbon materials make them ideally suited alternative to costly Pt counter electrode for their good catalytic activity, resistance to iodine corrosion, and high stability of the device. Apart from the extensively acclaimed photoanode TiO$_2$, BaSnO$_3$ (BSO) has been projected as an efficient alternative to it. In this study, remarkable efforts have been endeavoured to establish BSO-carbon-based DSSC device. Investigation on the adequate performance of natural source derived carbon-based counter electrode for BSO-based DSSCs, explored as a significant alternative to costly Pt and TiO$_2$, respectively, which could elucidate better photo-stability and more extended device performance compared to TiO$_2$-Pt-based DSSCs.

*Keywords: DSSC; BaSnO$_3$; Carbon; Counter Electrode; Photovoltaic*

## 1. Introduction

The trilemma of cost of energy, the security of supply, and human-made climate change are driving the move to the development and use of sustainable non-polluting energy sources that can also achieve low cost. While researching new ways to increase the efficiency of utilizing solar energy, technology is continuously being developed into new and better-advanced result. The discovery of dye-sensitized solar cells (DSSCs) in 1991 by Grätzel and co-workers stands out as one of the front-runners given the fundamental novelty of the concept derived from nature's principles [1]. The chemical way of assembling the cell architecture, which allows easy and cost-effective processing alternatives [2]. The current efficiency of DSSC reaches 14.2% [3]. The primary advantage of DSSCs lies on higher solar to electricity conversion efficiencies with lower production costs, flexibility and eco-friendliness. The efficiency can be enhanced in many ways such as light scattering effect of the photoanode materials, stability of the dye, using electron-transporting layer, enhancement of open-circuit voltage and fill factor and modification of DSSC device fabrication process [4]. In addition, the development of Pt-free counter electrode (CE) material can make DSSCs more competitive among various photovoltaic devices. An excellent CE material should possess (a) high stability and (b) high catalytic activity and Pt holds two properties; that is the reason for using it as the best CE material [5]. However, Pt is costly

---

* Corresponding author. Tel.: 01326 259486
*E-mail address:* A.Roy30@exeter.ac.uk; ar.chem30@gmail.com

and resulting in iodine corrosion. In this regard, attempts have been in progress to replace the costly Pt electrode with other cost-effective materials. Different nanostructured materials, including metal oxides, oxide perovskites and carbon-based composites, have been studied for photoanodes, and counter electrodes, which are crucial to achieving DSSC devices with higher efficiency and better stability. Many studies have been carried out to reduce the amount of Pt used in DSSCs and/or to explore alternatives to Pt, but mostly they deal with the $TiO_2$ based photoanode, which becomes stagnant and attained a limited area of research [6-8].

Carbon, which is one of the most abundant material in the earth's crust, is the best material to replace Pt. Mainly due to its core features like cost-effectiveness, environmental friendliness, availability, corrosion resistance and excellent catalytic activity towards the redox species. At the same time, the development of new materials as such carbon using cost-effective and abundant elements such as carbon for fabricating novel electrodes have also become technologically desirable [9-12]. Introduction of different carbon materials and device developments can significantly increase the regular performance of the conventional DSSC device. The different combinations in which carbon atoms can be arranged produce a wide variety of compounds that have unique and exciting physical, chemical, and electronic properties. Thus, carbon-based devices offer several attractive features for use in next-generation electronics. Ramuz et al. (2012) reported their efforts into the fabrication of the first reported all-carbon solar cell in which all components were carbon-based [13]. Similarly, Lee et. Al. (2012) described all-carbon counter electrodes for DSSCs. An efficient way to developed fibre-shaped DSSC based on an all-carbon electrode was also reported by Cai et. Al. (2012) [14]. However, the stability of these cells is yet to be studied for practical implementation.

Lesser electron mobility, higher dye absorption time, metal ion dye complex formation, interfacial charge recombination between a metal oxide, electrolyte and overall limited synthesis strategies are issued that restrict the scope of binary oxides in DSSCs [2]. In the search for alternative oxide to $TiO_2$, $BaSnO_3$ (BSO) exhibits different morphology, and interesting physicochemical properties, which can be established as a suitable alternative photoanode candidate for DSSCs [15, 16]. In this report, a systematic evaluation of the DSSCs performances of the cells fabricated with the facile, cheaper and more stable BSO-based photoanode with a carbon-based CE, the synthesized materials as an alternative to costly $TiO_2$ and Pt has been evaluated. At the same time, the performance of $TiO_2$ based photoanode with carbon counter electrodes are also taken into account and compared with the BSO-carbon system in DSSCs. To best of our knowledge, this may be the first time we report here the BSO-Carbon photoanode-CE combination as an alternative materials based system for DSSC application.


## 2. Materials and Methods

### 2.1. Development of carbon CEs for DSSC

To fabricate carbon-based CE, we have taken two different types of carbon; namely, glucose derived graphitic carbon sheet (GCS), and sesame oil derived graphitic carbon nanoparticles (GCP), the synthesis and various physiochemical characterizations of the synthesized carbon have been already reported in our previous publication [17, 18]. The synthesized powders have been now introduced to prepare CEs for DSSCs. Individually, 5.1 mg of synthesized carbon powder was added to 5 mg of Triton X-100 (Sigma Aldrich) in 3 mL of ethanol and stirred for 30 min, followed by ultrasonication for 1 h. Finally, the supernatant was carefully decanted and the rest of the part used for further process. The conductive side of a dried FTO was placed on the holder of a spin coater unit (Midas Spin-3000A, Korea) and the solution was spin-coated at 5500 rpm for 90 sec. We have repeated three cycles for the same and after that carefully washed with distilled water and baked for 30 min, at 120°C. The film was further dipped in 60 % $HNO_3$ (Merck, India) for 1h to enhance the electrical conductivity of the synthesized carbon powder and removal of Triton X-100. Finally, the spin-coated film was dried entirely under an infrared (IR) lamp and used as a CE in a DSSC device. The overall scheme of this study has been described in Fig. 1.
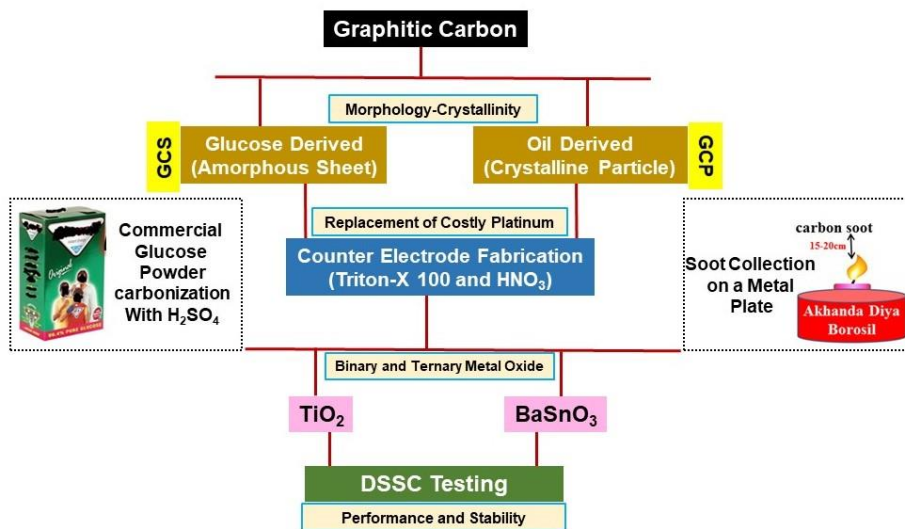
Fig. 1. Schematic illustration of the overall approach of this study.

## 2.2. Synthesis of BaSnO₃ nanoparticle

BaSnO$_3$ (BSO) nanoparticles were prepared as reported in the literature [15]. In short, 10 mM each of BaCl$_2$·2H$_2$O (Emsure, Merck, India) and SnCl$_4$·5H$_2$O (98% pure, Loba Chemicals, India) were thoroughly stirred under 30% H$_2$O$_2$ (Emparta, Merck, India) medium for 30 min to form a homogeneous solution. A 25% NH$_4$OH (Merck, India) solution was added dropwise to the mixed solution until the pH of the resultant solution reached 10. The solution was centrifuged at 10,000 rpm, and a white product was collected. The product was entirely dried under an IR lamp, and further calcined at 1000 °C for 8 h to produce the BaSnO$_3$ phase. The obtained powder was allowed to make a paste using ethyl cellulose and terpinol (Sigma Aldrich). Finally, the paste was used to prepare the photoanode using the screen printing method.

## 2.3. Material Characterizations

The Raman spectra have been performed on a STR500 (Cornes Technologies system by using 514.5 nm Ar$^+$ green laser with 50 mW power). The room temperature photoluminescence (PL) spectra with a steady-state spectrofluorometer (QM-40, Photon Technology International, PTI) using a 150 W xenon lamp as an excitation source, using 5 nm band-pass. Nitrogen physisorption measurements of all the samples were carried out by using a Quantachrome (iQ3) instrument after evacuation at 80°C for 2h. The specific surface area was calculated by the Brunauer-Emmett-Teller (BET) method, whereas desorption cumulative pore volume and pore size distribution were calculated by the Barrett-Joyner- Halenda (BJH) method. The morphology of the synthesized powder has been monitored on a Tecnai G2 30ST (FEI) high-resolution transmission electron microscope (TEM) operating at 300 kV. The transmittance spectra of the fabricated carbon films were measured on a UV-vis-NIR spectrophotometer (Shimadzu UV-3600). The surface microstructure of the fabricated carbon films was checked on a field emission scanning electron microscope (FESEM) (Supra 35VP, Carl Zeiss).

## 2.4. DSSC device assembly and testing

The TiO$_2$ paste (18 NR-T and 18 NR-O) was obtained from Dyesol(R), now known as Greatcell Solar. Ruthenium 535 bis-TBA (N719) dye, Pt electrode, and plastic spacer (Meltonix) were obtained from Solaronix, SA in this work.

The prepared I$^-$/I$_3$ electroluyte has been used for the devce testing.The complete assembling and final device fabrication protocol of the DSSC testing have been described in our previous report [15, 16]. The active area of the dye-coated BSO and TiO$_2$ film was 0.2826 cm$^2$. The only difference is instead of Pt electrode, we have used the fabricated carbon CEs in this study. Further, the photovoltaic testing of the fabricated DSSCs was executed under 1000 W.m$^{-2}$ of light from a Wacom AAA continuous solar simulator (model: WXS-210S-20, AM1.5G). The *I-V* characteristic of the devices was recorded using an EKO MP-160i *I-V* Tracer.

## 3. Results and discussions

### 3.1. TEM analysis

The transmission electron microscopic (TEM) images obtained from the as-prepared GCS sample are shown in Fig. 2a-c. The sample exhibited a layered elliptical sheet-like structure, with visible porosity as evident in the bright field images, as shown in Fig. 2a and Fig. 2b. The selected area electron diffraction (SAED) pattern of the as-prepared sheet appears amorphous, as shown in Fig. 2c. Similarly, the TEM images obtained from GCP sample has been shown in Fig. 2d-f. The particles exhibited chain-like structures as evident from Fig.2 d and Fig. 2e. The size of the individual carbon nanoparticles varied in the range of 20-45 nm and the average particle size varied as 30.5 ± 2nm. The corresponding SAED pattern suggests the absence of distinguishable lattice structures for carbon nanoparticle indicating a partially crystalline nature of individual carbon nanoparticles indicating (002) and (101) planes of graphitic carbon, respectively.
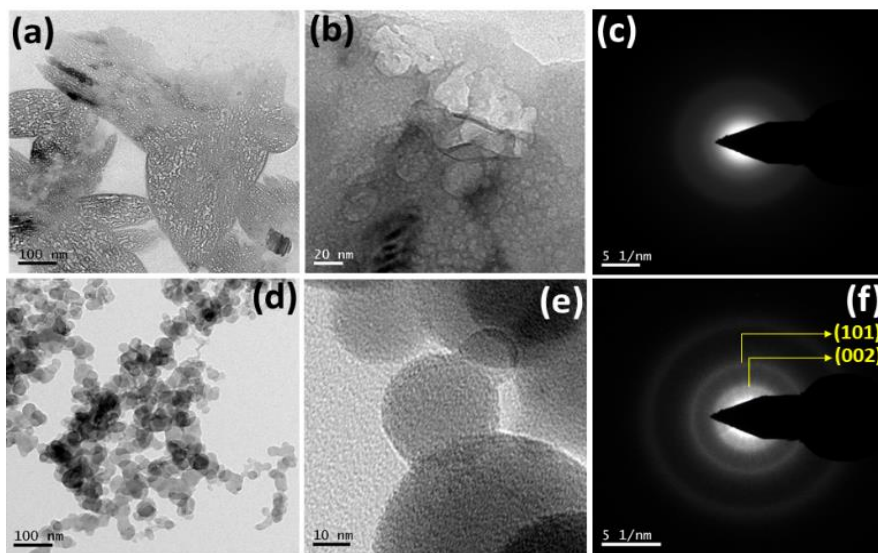


Fig. 2. TEM bright-field images of glucose-derived porous carbon sheet (a)-(b) at different magnification, (c) corresponding SAED pattern, (d)-(e) TEM bright-field images of sesame oil-derived carbon nanoparticles at different magnifications and (f) corresponding SAED pattern.

### 3.2. Optical and surface area analysis

To further evaluate the optical properties of the two different carbon material, the Raman and photoluminescence characteristics were studied. The Raman spectra of the synthesized carbons are presented in Fig. 3a. Raman spectrum of the GCS sample exhibits the characteristics graphite band (G) appearing at 1540 cm$^{-1}$, defect (D) for disorder band (sp$^3$) appearing at 1358 cm$^{-1}$ and G', or 2D band at 2896 cm$^{-1}$ dominate in the Raman spectrum of graphitic carbon nanoparticles. The G band corresponds to the high-frequency Raman active E$_{2g}$ mode (sp$^2$ carbon) of single-crystal graphite, and the broad D band corresponds to A$_{1g}$ mode arising out of disordered graphite and indicates the presence

of nanocrystalline graphitic nanoparticles [17, 18]. The $I_D/I_G$ ratio of around 0.883 confirms the graphitic nature of the synthesized carbon along with a broad 2D band, as shown in Fig. 3a. The existence of a broad 2D band could be a clear indication of the formation of disordered graphitic carbon with more graphene layers. In case of GCP sample, we have observed the G band around ~1586 cm$^{-1}$ and D band around ~1349 cm$^{-1}$ as appeared due to the presence of sp$^2$ and sp$^3$ kind of carbon with $I_D/I_G$ ratio of 0.9293, indicating a high degree of graphitization (Fig. 3a). This ratio is also a measure of the extent of the disorder and sp$^3$/sp$^2$ carbon atoms. There is also a starking difference in the full width at half maxima (FWHM) of both G and D bands of the synthesized carbon sample compared to that of the standard graphite powder. This broadening represents a direct indication of an increased level of disorder due to the presence of sp$^3$-G and a decrease in the graphitic domain size. The broadening of the D band also implies an increased level of disorder and a decrease in the graphitic domain size. The recombination of carbon bonds during carbon nanoparticle formation introduces smaller graphitic domains with a different bond. This could again be a clear indication of the formation of disordered graphitic carbon with more graphene layers. To gain insight into the optical properties of the prepared synthesized carbon samples, we carried out the fluorescence studies on the water dispersions of the particles at a pH of ~ 6.8. As evident from Fig. 3b, the most substantial emission maximum appeared at 458 nm upon 360 nm excitation exhibited excellent blue emission without any surface functionalization or surface treatment for glucose-derived carbon sheet. Whereas, the sesame oil-derived carbon nanoparticles exhibited excellent blue emission at a lower wavelength than the other one. The maximum UV emission occurred on 280 nm excitation, and the maximum visible emission occurred on 350 nm excitation. The most exciting feature of the PL of these samples is the explicit dependence of the excitation wavelength on both emission wavelength and intensity [18]. The distinct PL characteristics entirely generated due to the presence of defect mediated states (D and 2D band) and their different distribution in the synthesized carbon sample as observed from Fig. 3b. The zeta potential measurement result further indicates carbon sheets containing more surface-functionalized group form stable aqueous dispersion, whereas the nanoparticles are comparably weaker to form an aqueous dispersion. Though, in case of electrophoric mobility analysis, the later one shows higher value than the previous one may be due to discrete particle formation compared to the stacked sheet-like assembling. The comparative data has been tabulated in Table 1. Surface area analysis also plays a pivotal role in the catalytic activity of carbon. There is a significant difference in the BET surface area measurement. Due to multi-oriented distribution of the sheet-like structure and visible porosity appearance, the glucose derived carbon possess higher BET surface area and pore size of 140 m$^2$.g$^{-1}$ and 5-8 nm, respectively than sesame oil derived particle carbons where the later having the value of BET surface area and pore size distribution was 55 m$^2$.g$^{-1}$, and 10-20 nm, respectively (Table 1).
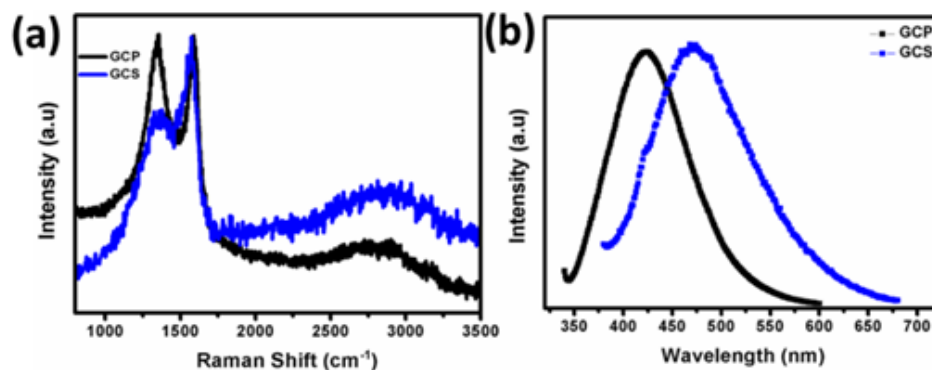


Fig. 3. (a) Raman and (b) photoluminescence spectra of GCP and GCS samples.

Table 1. Comparative physicochemical characteristics of synthesized carbon samples.

| Sample | Morphology | Zeta Potential (mV) | Electrophoric Mobility at 300K x $10^{-3}$ ($cm^2.V^{-1}s^{-1}$) | BET Surface Area ($m^2.g^{-1}$) | BJH Pore Size (nm) |
|--------|------------|---------------------|------------------------------------------------------------------|----------------------------------|--------------------|
| GCS | Sheet | -31.1 | 0.067 | 140 | 5-8 |
| GCP | Particle | -12.5 | 0.175 | 55 | 10-20 |

### 3.3. Characterization of the carbon films

FESEM microstructural analyses of the carbon films are shown in Fig. 4a and Fig. 4b. In the case of graphitic carbon series, the GCP film exhibits the porous exfoliated structure of the film surface as obtained from the FESEM analysis as shown in Fig. 4a. Agglomeration of particles may have resulted in the formation of a sheet-like continuous layer of carbon materials. Whereas, the GCS film exhibited a sheet like the one structure spread over the FTO surface and attained a high degree of porosity and surface area, as shown in Fig. 4b. It is also interesting to notice the transmittance spectra of the fabricated films (Fig. 4c). The effective performance can satisfy the compromise between efficiency and transparency of the cell. As per Fig. 4c, GCP films show higher order of transparency, ~60 % in the visible region (200-800 nm) than the GCS film where the transmittance of the film was observed ~50% at the same wavelength region. The digital images of respective carbon films along with the bare FTO glass, as shown in Fig. 4d indicates the relative transparency of the sample. Finally, the carbon electrodes were explored in DSSCs with BSO, and the result has been compared with the commercial $TiO_2$.
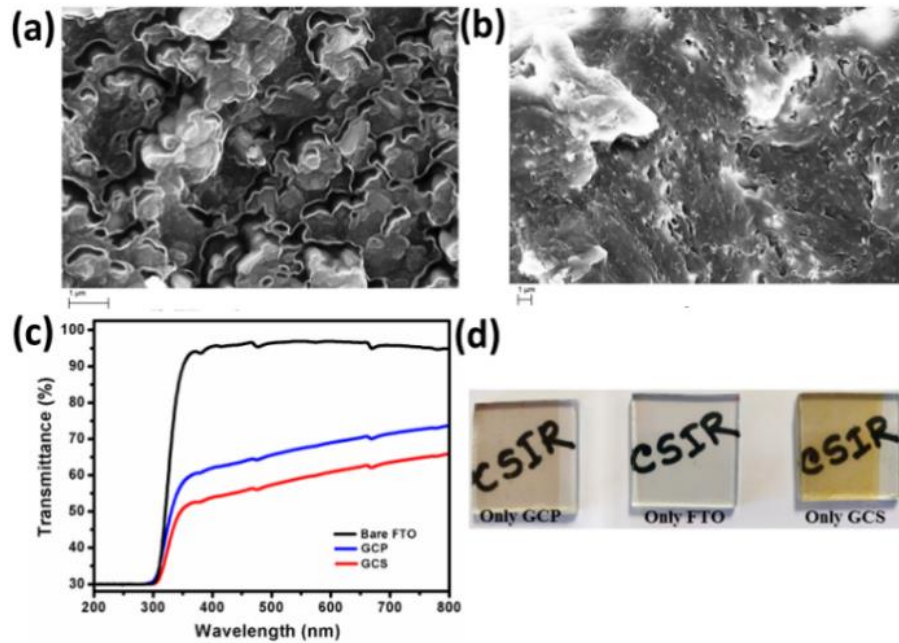


Fig. 4. FESEM images of (a) GCP, (b) GCS films, respectively, (c) Transmittance spectra of the GCP and GCS film compared with bare FTO glass and (d) digital images of fabricated films compared with bare FTO glass.

### 3.4. Photovoltaic performance of the carbon CEs

The comparative photovoltaic performance as *J-V* characteristics plot is shown in Fig. 5a and corresponding parameters for each of them have been further illustrated in Table 2. The fabricated GCP CE exhibited a maximum conversion efficiency (η) of 3.81 % with a short circuit current ($J_{SC}$) 9.60 $mA.cm^{-2}$, open-circuit voltage ($V_{OC}$) 0.74 V

and a fill factor (FF) of 0.54 for BSO based photoanode. On the contrary, with the same photoanode, the GCS counter electrode exhibited a $\eta$ of 2.24 % with a $J_{SC}$ 9.05 mA.cm$^{-2}$, $V_{OC}$ 0.84 V and FF of 0.64. At the same time, the GCP and GCS CEs were further tested with TiO$_2$-based devices, and maximum efficiency of 4.61 and 3.27 % were achieved, respectively. It has been observed that crystallinity does not make any significant effect on CE performance as seen from the performance of GCS and GCP based films. Instead, the performance more depends on the morphology and physicochemical properties. The *J-V* characteristics evaluate the TiO$_2$ based devices exhibit higher efficiency than the BSO based devices for both types of carbon CE. Among the two different carbon CEs, GCP films show enhanced performance for both the photoanodes than GCS film. The exciting fact is here to be noted that both the carbon-based devices exhibit a $V_{OC}$ of > 0.7 V for BSO-based photoanode, which is almost identical with the TiO$_2$-based photoanode. The results interpret that carbon-based CE performs superior for BSO compared to TiO$_2$ based photoanodes. In order to further understand the sufficient stability of the BSO-carbon based devices, we have further investigated the performance stability of the BSO-carbon device and compared with TiO$_2$-carbon device over 30 days, as shown in Fig. 5b. The efficiency of the TiO$_2$ based devices was drastically depleted for both the GCP and GCS films. Whereas, there is a steady reduction in efficiency was observed in the case of BSO-based devices for carbon films. Besides, the photovoltaic performance of GCP CEs finds better compared to GCS CE and therefore, has been selected for the photo-stability study.

We recorded the device performance as a function of illumination time under constant light power, as illustrated in Fig. 5c and Fig. 5d. We are interested in looking at the $J_{SC}$ and $V_{OC}$ and observed that BSO-GCP devices do not degrade over time with light soaking. Whereas, TiO$_2$-GCP devices show comparatively faster degradation in $J_{SC}$. (Fig. 5c). We recall that the photo-degradation in the $J_{SC}$ was attributed to the formation of light-activated metastable trap states and their accumulation in the dye layers over a long duration, resulting in a slight decrease of photocurrent overtime under 1 SUN illumination condition [19]. The $V_{OC}$ measurements exhibit excellent stability of BSO-GCP devices compared to TiO$_2$-GCP devices as observed up to 10 h constant 1 SUN illumination without additional UV filters, as shown in Fig. 5d. The overall degradation may cause due to an increase in temperature of the solar cell on constant illumination of 1 SUN [20]. Therefore, as per the overall observation from Fig. 5, as an alternative new material, the BSO-GCP device pair could be a promising competitor to TiO$_2$-Pt in terms of photo-stable and cheaper material for DSSCs.
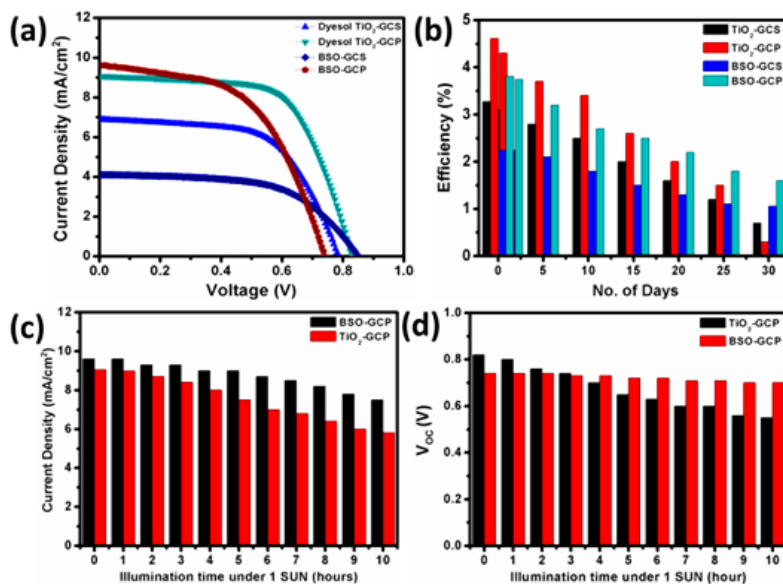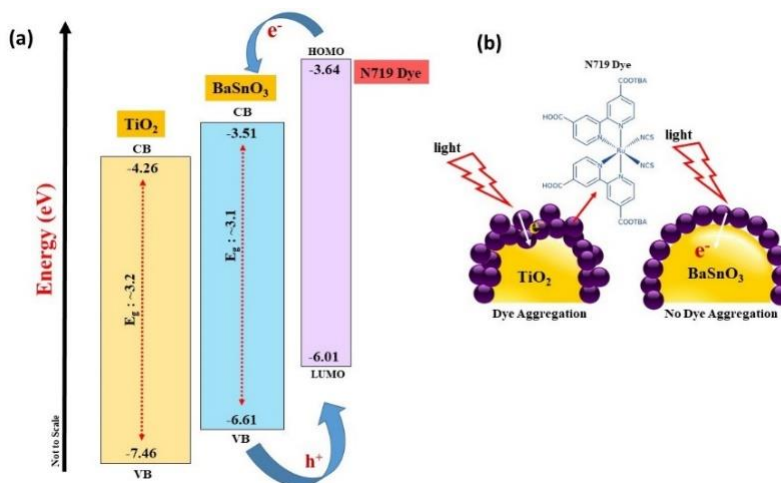


Fig. 5. (a) Current density-voltage characteristics plot, (b) efficiency stability plot of GCP and GCS counter electrodes for TiO$_2$ and BSO-based DSSC devices, respectively, (c) and (d) comparative plot of current density ($J_{SC}$) and open-circuit voltage ($V_{OC}$) of the BSO-GCP and TiO$_2$-GCP cells under constant 1 SUN 1.5 AM illumination for 10 h.

Table 2.  Photovoltaic performance of carbon CEs for TiO$_2$ and BSO-based DSSCs.

| Device (Photoanode-CE) | J$_{SC}$ ±0.2 (mA/cm$^2$) | V$_{OC}$ (V) | FF | PCE (%)±0.2 |
|---|---|---|---|---|
| TiO$_2$-GCS | 6.88 | 0.78 | 0.61 | 3.27 |
| TiO$_2$-GCP | 9.05 | 0.82 | 0.64 | 4.61 |
| BSO-GCS | 4.11 | 0.84 | 0.64 | 2.24 |
| BSO-GCP | 9.60 | 0.74 | 0.54 | 3.81 |

Fig. 6a illustrates the electronic bandgap (E$_g$) alignment diagram of BSO and TiO$_2$, along with the N719 dye. In term of the E$_g$ alignment, the conduction band (CB) of BSO places in a higher position compared to the CB of TiO$_2$ and bring closure to the HOMO (highest energy occupied molecular orbital) of the N719 dye molecule [21]. Actually, for BSO, the CB reveals a highly dispersed band structure leading to a small effective mass and high mobility of electrons [22]. This implies that the electrons in the conduction band of BSO can diffuse rapidly, which is also consistent with the above results. The rapid electron capture of the BSO photoanode is beneficial for efficient DSSC development.

In addition, it is anticipated that due to the higher the cathodic peak current density, carbon shows better the catalytic activity as a CE compared to Pt [23]. Besides, acidic dye aggregations turned out as a significant factor, which might be hindered the smooth diffusion of the electrons and restrict interpenetration of electrolyte through making blockage into the pores as well as the surface of the TiO$_2$ affecting the electron transportation process of the device severely as shown in Fig. 6b. The formation of the inhomogeneous metal-dye complex on the surface changes the surface properties from comparatively hydrophobic to hydrophilic nature and thus degrade the performance [24, 25]. BSO-based photoanode is relatively stable to this type of acidic dyes and does not allow any dye blockage, leading to provide stability to the device.



Fig. 6. Schematic diagram of (a) energy band alignment to TiO$_2$, BaSnO$_3$ with the N719 dye (where HOMO: Highest energy occupied molecular orbital; LUMO: Highest energy occupied molecular orbital; VB: Valence band; CB: Conduction band; E$_g$: Bandgap) and (b) N719 dye interaction occurs at the surface of TiO$_2$ and BaSnO$_3$ photoanodes.

## 4. Conclusion

In conclusion, the development of carbon-based material develops an efficient replacement of the Pt-free counter electrode material, which can make DSSCs more competitive among various photovoltaic devices. Significant results of various carbon counter electrodes were further extracted with one of the major leading alternative photoanodes such as $BaSnO_3$ (BSO). Natural source derived carbon material series, 3.81 % (GCP) and 3.27 % (GCS) efficiencies were observed for BSO-based DSSC. Besides, we have monitored our results with the $TiO_2$ based photoanodes systems. We found that BSO-GCP devices exhibit better stability than $TiO_2$-GCP devices. The later relatively undergoes faster photo-degradation in photocurrent and open-circuit voltage and therefore efficiency. Through this work, we show that improving the crystalline quality of the physicochemical characteristics and synthesis of carbon material leads to create a more reliable interface of charge carrier transport with BSO rather $TiO_2$ for DSSCs. Altogether, this constitutes an important step toward achieving photo-stable alternative material based DSSC devices for futuristic conceivable optoelectronic applications. The performance of various non-Pt based counter electrode materials can exhibit a significant performance and more efficiency on proper modification and optimization of the fabrication process. Thus, the development and evaluation of new organic and inorganic compounds as an alternative material to Pt in DSSCs is a promising research area, which is essential to reduce the cost of the devices for commercialization.

## Acknowledgements

## Conflict of interest

The authors declare no conflict of interest.

## References

[1] B. O'Regan, M. A. Grätzel, Nature 353 (1991) 737-740.
[2] J. Gong, K. Sumathy, Q. Qiao, Z. Zhou, Renew. Sust. Energ. Rev. 68 (2017) 234-246.
[3] J-M. Ji, H. Zhou, Y. K. Eom, C.H. Kim, H.K. Kim, Adv. Energy Mater. 10 (2020), 2000124.
[4] K. Sharma, V. Sharma, S.S. Sharma, Nanoscale Res. Lett. 13 (2018) 381.
[5] S. Thomas, T. G. Deepak, G. S. Anjusree, T. A. Arun, S.V. Naira, A. S. Nair, J. Mater. Chem. A 2 (2014) 4474-4490.
[6] S. Yun, P. D. Lund, A. Hinsch, Energy Environ. Sci. 8 (2015) 3495-3514.
[7] A. Roy, P.S. Devi, S. Karazhanov, D. Mamedov, T.K. Mallick, S. Sundaram, AIP Advances 8 (2018) 070701.
[8] B. Lee, D. Buchholz, R. Chang, Energy Environ. Sci. 5 (2012) 6941-6952.
[9] E. Meyer, R. Taziwa, D. Mutukwa and N. Zingwe, Metals 8(12) (2018) 1080.
[10] S. Yun, A. Hagfeldt, T. Ma, Adv. Mater. 26 (2014) 6210-6237.
[11] J. D. Roy-Mayhew, I. A. Aksay, Chem. Rev. 114 (12) (2014) 6323-6348.
[12] A. Roy, A. Ghosh, S. Bhandari, S. Sundaram and T.K. Mallick, Ind. Eng. Chem. Res. 59 (2020), 11063-11071.
[13] M.P. Ramuz, M. Vosgueritchian, P. Wei, C. Wang, Y. Gao, Y. Wu, Y. Chen, Z. Bao, ACS Nano 6 (2012) 10384-10395.
[14] X. Cai, S. Hou, H. Wu, Z. Lv, Y. Fu, D.Wang, C. Zhang, H. Kafafy, Z. Chu, D. Zou, Phys. Chem. Chem. Phys. 14 (2012) 125-130.
[15] A. Roy, P.P. Das, P. Selvaraj, S. Sundaram, P. S. Devi, ACS Sustainable Chem. Eng. 6 (2018) 3299-3310.
[16] A. Roy, P. Selvaraj, P. S. Devi, S. Sundaram, Mater. Lett. 219 (2018) 166-169.

[17] A. Roy, S. Chatterjee, S. Pramanik, P.S. Devi, G.S. Kumar, Phys. Chem. Chem. Phys. 18 (2016) 12270-12277.

[18] P.P. Das, S. Pramanik, S. Chatterjee, A. Roy, A. Saha, P. S. Devi, G. S. Kumar, ACS Sustainable Chem. Eng. 6 (2018) 10127-10139.

[19] P. Salvador, M. G. Hidalgo, A. Zaban, J. Bisquert, Phys. Chem. B 109 (2005) 15915-15926.

[20] I. J. Junger, D. Werner, E. Schwenzfeier-Hellkamp, A. Ehrmann, Optik 177 (2019) 8-12.

[21] D.W. Kim, S.S. Shin, S. Lee, I.N. Cho et al. Chem. Sus. Chem. 6 (2013) 449-454.

[22] N. Rajamanickama, P.  Soundarrajan, K. Jayakumara, K. Ramachandran, Sol. Energy Mater. Sol. Cells 166 (2017) 69-77.

[23] S. Gnanasekar, P. Kollu, S.K. Jeong et al. Sci Rep 9 (2019) 5177.

[24] J. S. Shaikh, N. S. Shaikh,  S. S. Mali, J. V. Patil et al. Nanoscale 10 (2018) 4987-5034.

[25] K. Fan, J. Yu, W. Ho, Mater. Horiz. 4 (2017) 319-344.